

Eigengalaxies: describing galaxy morphology using principal components in image space

Emir Uzeirbegovic,[★] James E. Geach and Sugata Kaviraj

Centre for Astrophysics Research, School of Physics, Astronomy & Mathematics, University of Hertfordshire, Hatfield, AL10 9AB
Centre of Data Innovation Research, School of Physics, Astronomy & Mathematics, University of Hertfordshire, Hatfield, AL10 9AB

6 June 2022

ABSTRACT

We demonstrate how galaxy morphologies can be represented by weighted sums of ‘eigengalaxies’ and how eigengalaxies can be used in a probabilistic framework to enable principled and simplified approaches in a variety of applications. Eigengalaxies can be derived from a Principal Component Analysis (PCA) of sets of single- or multi-band images. They encode the image space equivalent of basis vectors that can be combined to describe the structural properties of large samples of galaxies in a massively reduced manner. As an illustration, we show how a sample of 10,243 galaxies in the *Hubble Space Telescope* CANDELS survey, which have visual classifications from Galaxy Zoo, can be represented by just 12 eigengalaxies whilst retaining 96% explained variance. We show how the emphasis of certain eigengalaxy components correspond to visual features (e.g. disc, point source, etc.), and explore the correspondence between combinations of eigengalaxies and features defined in the Galaxy Zoo-CANDELS catalogue. We also describe a probabilistic extension to PCA (PPCA) which enables the eigengalaxy framework to assign probabilities to galaxies and characterise a whole population as a generative distribution. We present four practical applications of the probabilistic eigengalaxy framework that are particularly relevant for the next generation of large imaging surveys: we (i) show how low probability galaxies make for natural candidates for outlier detection (ii) demonstrate how missing data can be predicted (iii) show how a similarity search can be performed on exemplars (iv) demonstrate how unsupervised clustering of objects can be implemented.

Key words: methods: data analysis, methods: statistical, galaxies: structure, techniques: image processing

1 INTRODUCTION

The distribution of light in galaxies, commonly referred to as galaxy ‘morphology’, is a fundamental observable property. Morphology strongly correlates with the physical properties of a galaxy, such as its stellar mass (e.g. Bundy et al. 2005), star formation rate (e.g. Bluck et al. 2014; Smethurst et al. 2015; Willett et al. 2015), surface brightness (e.g. Martin et al. 2019), rest frame colour (e.g. Strateva et al. 2001; Skibba et al. 2009; Bamford et al. 2009) and local environment (e.g. Dressler et al. 1997; Postman et al. 2005) and reveals key information about the processes that have shaped its evolution over cosmic time (e.g. Martin et al. 2018b; Jackson et al. 2020). For example, the smooth light distributions of elliptical galaxies, which are a result of the largely random orbits of their stars (e.g. Cappellari et al. 2011), are signposts

of a merger-rich evolutionary history (e.g. Conselice 2006). On the other hand, the presence of a disc indicates a relatively quiescent formation history, in which the galaxy has grown primarily through accretion of gas from the cosmic web (Codis et al. 2012; Martin et al. 2018a). In a similar vein, morphological details such as extended tidal features suggest recent mergers and/or interactions (e.g. Kaviraj 2014; Kaviraj et al. 2019; Jackson et al. 2019), with the surface brightness of these tidal features typically scaling with the mass ratios of the mergers in question (e.g. Peirani et al. 2010; Kaviraj 2010).

Apart from being a fundamental component of galaxy evolution studies, morphological information has a wide range of applications across astrophysical science. For example, it can be a key prior in photometric redshift pipelines (e.g. Soo et al. 2018; Menou 2018) which underpin much of observational cosmology and weak lensing studies, is used as contextual data in the classification of transient light curves

[★] e.uzeirbegovic@herts.ac.uk

(e.g. Djorgovski et al. 2012; Wollaeger et al. 2018) and is an essential ingredient in the study of the processes that drive active galactic nuclei (e.g. Schawinski et al. 2014; Kaviraj et al. 2015). The morphological analysis of galaxy populations, especially in the large surveys that underpin our statistical understanding of galaxy evolution, is therefore of fundamental importance.

A vast literature exists on methods for measuring galaxy morphology. Popular techniques range from those that describe a galaxy’s light distribution using a small number of parameters (e.g. de Vaucouleurs 1948; Sérsic 1963; Simard et al. 2002; Odewahn et al. 2002; Lackner & Gunn 2012) to non-parametric approaches such as ‘CAS’ (e.g. Abraham et al. 1994; Conselice 2003; Menanteau et al. 2006) or Gini- M_{20} (e.g. Lotz et al. 2004; Scarlata et al. 2007; Peth et al. 2016), where the light distribution is reduced to a single value. The convergence of large observational surveys and rapidly increasing computing power has recently brought machine learning to the fore in morphological studies. While the use of machine learning can be traced back at least as far back as the 1990s (e.g. Lahav et al. 1995), there has been a recent explosion of studies that apply such techniques to the exploration of galaxy morphology, particularly in large survey datasets (e.g. Huertas-Company et al. 2015; Ostrovski et al. 2017; Schawinski et al. 2017; Hocking et al. 2018; Goulding et al. 2018; Cheng et al. 2019; Martin et al. 2020).

Automated techniques lend themselves particularly well to the analysis of large surveys, but the most accurate method of morphological classification is arguably visual inspection (e.g. Kaviraj et al. 2007). Indeed the genesis of this subject can be traced back to the visual ‘tuning-fork’ classifications by Hubble (1926), where galaxies were classified into a so-called sequence of ellipticals and spirals. It is remarkable that this classification system still underpins the broad morphological classes into which galaxies are split in modern studies of galaxy evolution. Although visual inspection of large observational surveys is time-intensive, the advent of massively distributed systems like Galaxy Zoo has revolutionised its use on survey datasets (e.g. Lintott et al. 2011; Simmons et al. 2017; Willett et al. 2017). Galaxy Zoo has used more than a million citizen-science volunteers to classify large contemporary surveys, like the Sloan Digital Sky Survey (SDSS) and the *Hubble Space Telescope* (*HST*) Legacy Surveys and has provided the benchmark against which the accuracy of automated techniques have been routinely compared (e.g. Huertas-Company et al. 2015; Dieleman et al. 2015; Beck et al. 2018; Walmsley et al. 2019; Ma et al. 2019).

Principal component analysis (PCA) is a multivariate statistical technique used to convert a set of variables to a set of uncorrelated variables termed principal components (PCs). The PCs are defined iteratively such that each component accounts for the most possible remaining variance in a dataset and is orthogonal to all prior components. We consider the line of approach inspired by the work of Sirovich & Kirby (1987), in which they coined the term ‘eigenfaces’ as a synonym for the eigenvectors (presented as images) that result from a PCA decomposition of a set of 2D images, considered together as the row vectors of a common matrix. Those authors showed that a set of $N \times N$ images described as vectors in N^2 -space could be projected to a comparatively small M -space whilst preserving the majority of the

variance. The M basis vectors of the M -space became the template eigenfaces, where each face image in the original set could be faithfully reconstructed as a linear combination of the templates.

Similar methods have been applied in astronomy. For example, De La Calleja & Fuentes (2004) used PCA to project a set of 310 disparate images to a lower rank space to facilitate further classification steps. They referred to the basis eigenvectors as ‘eigengalaxies’ and used their weightings to test multiple machine learning methods against each other for the purpose of galaxy classification. Li et al. (2005) used PCA to decompose stellar spectra from the STELIB spectroscopic stellar library (Le Borgne et al. 2003) and Two Micron All Sky Survey (2MASS, Skrutskie et al. 2006) near-infrared photometry to derive ‘eigenspectra’ and then used them to fit the observed spectra of a selection of galaxies from the SDSS (Fukugita et al. 1996) Data Release 1. Anderson et al. (2004) generated many galaxies from a parametric model, calculated the eigenvectors of the generated set, and then used the reduced eigenspace to find the nearest synthetic model to any given real galaxy image as a way of discovering correspondence between galaxies and known structures. Wild et al. (2014) used PCA to concisely describe a large number of model spectral energy distributions (SEDs). They termed the retained eigenvectors as ‘super-colours’ and used them to impute SEDs from sparse samples in observed galaxies.

In this paper, we further consider the utility of PCs in image space, working with multi-band imaging and focusing on galaxy morphology. We start by finding a concise variance-preserving latent space representation using PCA, and as others have done before, refer to the resultant eigenvectors as ‘eigengalaxies’. Taking this concept further, we show how the result can be converted into a generative model which can assign likelihoods to galaxies, and demonstrate how the model enables the simple and principled implementation of a set of cross-cutting applications that may be of use to the community in a variety of scenarios, not necessarily limited to galaxy morphology studies.

The paper is structured as follows. In Section 2 we describe both the sample and our methodology and discuss the interpretation of eigengalaxies and its relevance to the interpretation of galaxy morphology. We then show how this result is converted to a generating distribution using probabilistic PCA (PPCA). In Section 3 we show how this probabilistic eigengalaxy framework leads to principled approaches in various applications. In particular, we (i) show how low probability galaxies make for natural candidates for outlier detection (ii) show how missing data can be predicted (iii) demonstrate how similarity searches for images can be implemented given an exemplar (iv) demonstrate how a natural unsupervised clustering of objects can be produced. We then outline how the methods may be used together in more advanced applications and how it is relevant to big datasets such as the upcoming Large Synoptic Survey Telescope (LSST) project (Robertson et al. 2017). Section 4 concludes and summarises our findings, and provides a link to the codes developed for this work.

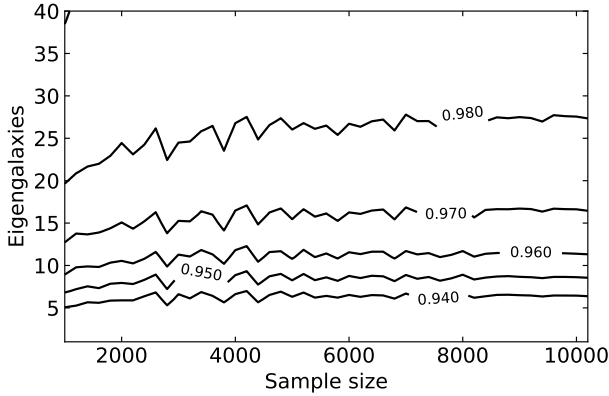


Figure 1. Contour plot of explained variance corresponding to the required number of eigengalaxies versus sample size. Higher explained variances tend to require proportionally more eigengalaxies as sample size increases, however at roughly 96% explained variance is asymptotic to a constant.

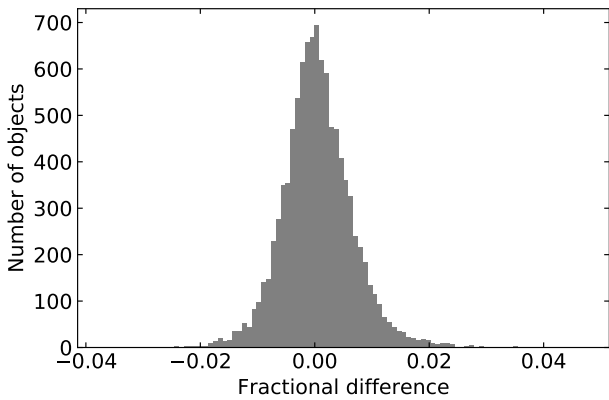


Figure 2. Histogram showing the frequency of the ratio of the sum of deltas (difference between original and reconstructed pixel flux over all bands) and the sum of the flux in the original images, for the PCA decomposition of the 10,243 galaxies in the GZ-CANDELS GOODS-S sample. 99% of objects lie between $\pm 2.5\%$. We account for 96% of variance by design and the distribution above shows that the reconstructed images bear a good likeness (in terms of reconstructed flux) to the originals.

2 EIGENGALAXIES

2.1 Data from *HST* CANDELS

HST CANDELS (Grogin et al. 2011; Koekemoer et al. 2011) offers a high-resolution probe of galaxy evolution. The survey consists of optical and near-infrared (WFC3/UVIS/IR) images from the Wide Field Camera 3 (WFC3) and optical images from the Advanced Camera for Surveys (ACS) in five well-studied extragalactic survey fields. Here, we focus on GOODS-S, one of the deep tier (at least four-orbit effective depth) fields. We select a sample of 10,243 galaxies present in the ‘Galaxy Zoo: CANDELS’ (GZ-CANDELS) GOODS-S catalogue (Simmons et al. 2016), that fall within the region jointly covered by the F814W, F125W and F160W bands.

The majority of objects are at $z < 3$ (Simmons et al. 2016). The motivation for using the GZ-CANDELS catalogue is that our results can be interpreted in the context of the morphological and structural classifications provided by the Galaxy Zoo citizen science project.

2.2 Object registration and preparation

The aim of registration is to remove the uninteresting sources of variation which would otherwise increase the number of eigengalaxies required. We identify pixel scale matching, image centering, cropping, range clipping and image rotation as the most important confounders to account for. For each object in the catalog we take a $1.8''$ cut-out, using the catalogued sky coordinate as a centroid. ACS images are down-sampled by a factor of two to match the pixel scale of the WFC3 images ($0.06''$ pixel $^{-1}$), so that for each band we obtain a 30×30 -pixel image at the position of each galaxy. The cut-out dimensions are selected with prior experimentation because they result in the least superfluous background for most targets.

We perform some simple post-processing to the data. In particular, we truncate the pixel distribution at the 99th percentile to avoid anomalous spikes in flux in some galaxies from accounting for too much variance. Next, we produce a temporary composite image of the array by using, for each pixel, its maximum magnitude across all bands. We then use the locations of all pixels in our composite with values exceeding the 75th percentile to create a matrix of the coordinates of bright pixels. The first principal component of the two column matrix of pixel coordinates is a vector of weights (x_0, y_0) which can be interpreted as the linear transformation of our 2D coordinates to the 1D space that preserves most variance (i.e. some line passing through the origin of the original 2D space). The angle between the original x -axis in our image and the new variance-preserving one is then given by $\theta = \arctan2(y_0, x_0)$. Finally, we transform the original array by rotating every band in turn by $\theta - \pi/2$ radians (in order to make vertical what would otherwise be a rotation to the horizontal plane) which results in vertically-aligned brightness.

2.3 Decomposition

The set of objects, each a registered $30 \times 30 \times 3$ array, are flattened into 1×2700 row vectors and concatenated to form a feature matrix. We perform PCA¹ on the resultant matrix, but prior to that we conduct some experiments to determine a reasonable level of explained variance to target. In theory, in the worst case scenario, as the ratio of explained variance approaches unity, the number of eigengalaxies required may be close to the total sample size. We perform PCA for varying sample sizes and create a contour plot to depict the relationship between sample size and the number of eigengalaxies required for any given level of explained variance (Figure 1). The n^{th} eigenvector is always the same regardless of what explained variance is targeted, because eigenvectors are ordered by explained variance and orthogonal to each other, so targeting a higher explained variance

¹ We use the Python package `sklearn.decomposition.pca`.

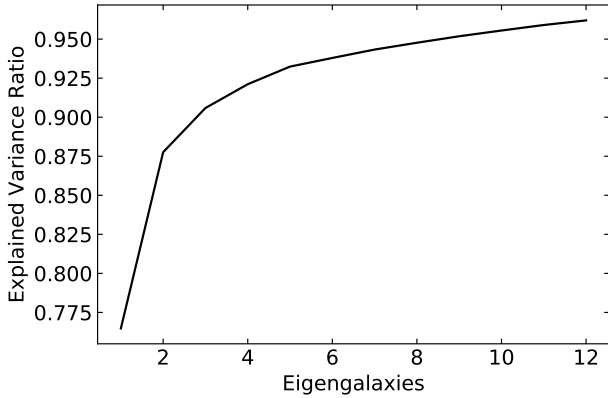


Figure 3. Cumulative explained variance illustrating how much variance each additional feature accounts for. In PCA successive components account for less variance than the previous component. In this instance, only *two* eigengalaxies are required to account for ~85% of explained variance yet 12 eigengalaxies are required to account for 96% of explained variance.

just means retaining more eigenvectors. We aim to target the highest level of explained variance asymptotic to a constant number of eigengalaxies as the sample size increases. This is important because we intend the methods illustrated here to be applicable to very large datasets in which the number of eigengalaxies targeted would have to be on an asymptotic curve. This is discussed further in Section 3. After choosing a target variance, each 1×2700 eigenvector is reshaped into a $30 \times 30 \times 3$ array: these are the eigengalaxies. Reshaping the previously flattened array is done by filling a $30 \times 30 \times 3$ array one band at a time in column order. The matrix of coefficients defining how the eigengalaxies are combined to reconstruct any given galaxy is termed the ‘score matrix’ and is also calculated.

2.4 Results and interpretation

Figure 1 presents a contour plot of explained variance corresponding to various combinations of sample size and eigengalaxy number. We chose to retain 96% variance as it is the highest target variance with near zero or asymptotic growth as sample size increases. Only 12 eigengalaxies were required to achieve an explained variance of approximately 96% for 10,243 objects. Let F_0 be the collection of flux densities of the pixels in the original images and F_Δ be the corresponding differences in flux between the original pixels and those in images reconstructed using the eigengalaxies. Figure 2 presents a histogram of $\sum_{x \in F_\Delta} x / \sum_{x \in F_0} x$ (i.e. the ratio of the sum of deltas and the sum of flux over all bands). It shows a symmetrical distribution centred at zero. 99% of objects lie between $|\sum_{x \in F_\Delta} x / \sum_{x \in F_0} x| < 2.5\%$.

Figure 3 shows the cumulative variance explained by successive eigengalaxies. PCA successively maximises the variance in each orthogonal eigengalaxy and each additional eigengalaxy therefore accounts for less variance. In this instance, only *two* eigengalaxies are required to account for ~85% of explained variance, yet 12 eigengalaxies are required to account for 96% of explained variance. Figure 4

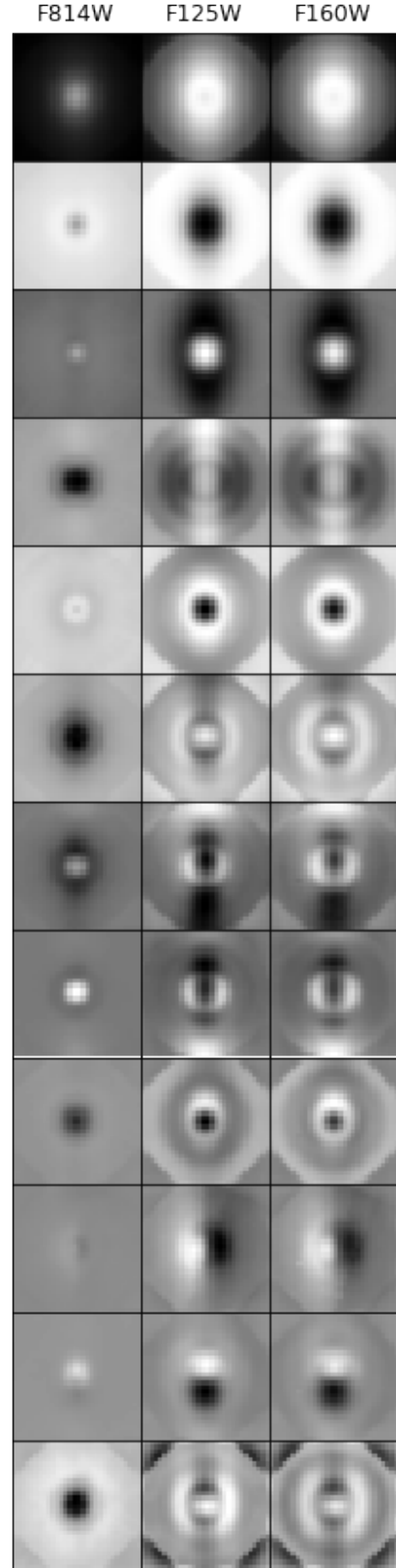


Figure 4. The 12 eigengalaxies accounting for 96% variance in the GZ-CANDELS GOODS-S sample. Each row is as an eigengalaxy and each column is a band. All images are scaled identically, where white indicates relative emphasis and black indicates relative de-emphasis of the region. Each image is 30×30 pixels, or $1.8'' \times 1.8''$.

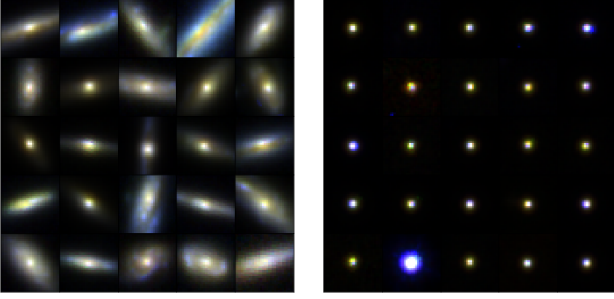


Figure 5. The left panel shows a sample of objects where eigengalaxy component 3 has an extreme negative weight, illustrating how different eigengalaxy components can correspond to visual features. In this case, eigengalaxy 3 seems to correspond to resolved disc-like structures, which are completely absent in the images in the right panel, which are point sources. Each 1.8'' thumbnail image is an RGB composite of the F160W, F125W, and F814W bands.

presents the 12 eigengalaxies as grayscale images. The effect of image rotation to vertically align brightness can be seen in the relative emphasis of the central vertical strip. One may also wonder how structure with high spatial frequency – such as spirals – would be reconstructed given the features of the eigengalaxies. Finessed features are a function of co-ordination of adjacent pixel columns and although visually distinct typically account for a tiny amount of flux variance. Therefore, fine-structured spiral features (for example) will become washed out in reconstructions, and not appear as sharp as in the real image.

Examining the first two eigengalaxies we see that they are intensity dominated. It is unsurprising that most variance is to be found in accounting for relative brightness, given the GZ-CANDELS sample spans (*H*-band) magnitudes down to $F160W < 28.3$ mag (Simmons et al. 2016). Subsequent eigengalaxies become more complex and structured. How can we interpret them? It is sometimes difficult to ‘eyeball’ the feature implications of any given eigengalaxy but it can be made clearer by contrasting samples which extremely emphasise ($>99^{\text{th}}$ percentile) or de-emphasise ($<1^{\text{st}}$ percentile) the eigengalaxy as shown in Figure 5. In this example, it appears that extreme negative weights on eigengalaxy component 3 corresponds to the presence of extended resolved features such as (but not exclusively) discs; conversely, extreme positive eigengalaxy 3 weights result in point sources with no, or insignificant, resolved structure. Thus, selection on relative component weighting could lead to practical applications such as star/galaxy separation or the identification of quasars.

Where individual eigengalaxies do not coincide with a feature of interest, the correspondence can be sought with a combination of eigengalaxies. One way to establish this correspondence is to train a classifier to discover the relationship between the eigengalaxy scores and a set of labels, and then to interpret the classifier to better understand the correspondence. Note that the performance of classifiers for use cases such as these will be substantially dependent on the purity of labelled classes in the training set. We match the number of galaxies in each class to make the *ex ante* probability of any class roughly equal. We reserve half of

the data at random for training, withhold the other half for testing, and fit a random forest (Liaw et al. 2002) classifier using the GZ-CANDELS classifications as a response and the score matrix as the explanatory variables. The random forest classifier is an ensemble learning technique which aggregates the classifications of a large number of decision trees. Decision trees themselves have low bias but a high variance on out of sample predictions because they tend to over-fit data. The random forest corrects for this by randomly partitioning the data that each tree can see, which has the effect of de-correlating tree classifications. The mean or mode of the resultant tree classifications is then used to produce the final result. Random forests can have a drastically lower variance than that of a single decision tree fitting, whilst retaining much of a decision tree’s interpretability.

Figure 6 shows the error matrix (a cross tabulation of true class labels versus predicted class labels) for the withheld data. Correspondence to complex GZ-CANDELS rules is good despite some inherent class ambiguity. GZ-CANDELS classifications are based on combinations of cut-off points corresponding to fractions of votes by human classifiers. Classifications are presented as mutually exclusive whereas it is possible for a spiral galaxy to be simultaneously edge-on and/or clumpy for example, leading to classification ambiguity. Figure 7 illustrates the importance weighting for each eigengalaxy in random forest classifications. It shows a particular emphasis on a subset of the eigengalaxies when classifying edge-on, spiral and clumpy galaxies against each other.

The eigengalaxies themselves encode something elementary about the (usually) complex multi-band light distribution in the transformed galaxy sample, and therefore can be used in a sense to ‘define’ morphology in a non-parametric, data-driven way through the score matrix, where the assumptions of PCA are reasonable; that is, that features are orthogonal, with each maximising the remainder of the residual variance, and the dataset is well described by a mean and covariance structure.

2.5 PCA as a generative model

Extending PCA to a probabilistic generative model greatly enhances its capabilities to applications like predicting missing data, generating new data and drawing inferences about the likelihood of data, which PCA alone is not capable of. Tipping & Bishop (1999b) show that PCA is equivalent to the maximum likelihood (ML) solution of the factor model, which aims to map an observed vector space to an unobserved latent space by a linear transformation: $t = Wx + \mu + \epsilon$. Here $t \in \mathbb{R}^d$ is the observation vector, $x \in \mathbb{R}^q$ is the latent vector, W is a $d \times q$ loading matrix (the coefficients mapping an observed vector to the latent space) relating t to x where $q < d$, μ is an offset and ϵ is a residual error. Tipping & Bishop (1999b) show that given $x \sim N(0, I)$, and $\epsilon \sim N(0, \sigma^2)$ (i.e. isotropic error), then $t \sim N(\mu, WW^T + \sigma^2 I)$, and the ML solution yields W equivalent to the eigenvectors of the covariance matrix (the PCA decomposition).

Given a PCA decomposition and an ML estimate of σ^2 , the established equivalence means that we can write down a generative factor model. This offers two key opportunities further discussed later: (i) the factor model is Gaussian and we can simultaneously estimate the loading matrix and miss-

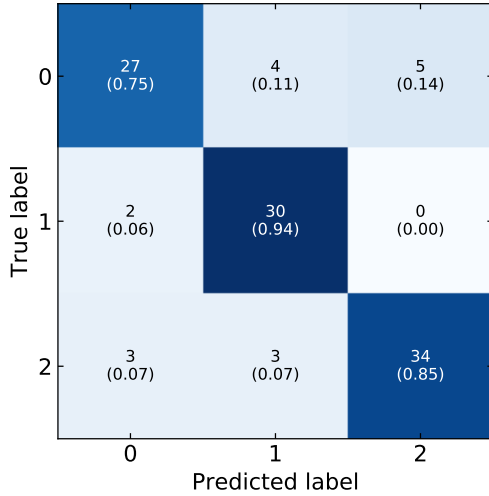


Figure 6. Error matrix depicting the correspondence between true labels and those predicted by a random forest for edge-on (0), spiral (1) and clumpy (2) galaxies. It shows good ($\gtrsim 75\%$) correspondence to GZ-CANDELS classification rules which are based on Boolean combinations of cut-off conditions for fractions of user votes on different features.

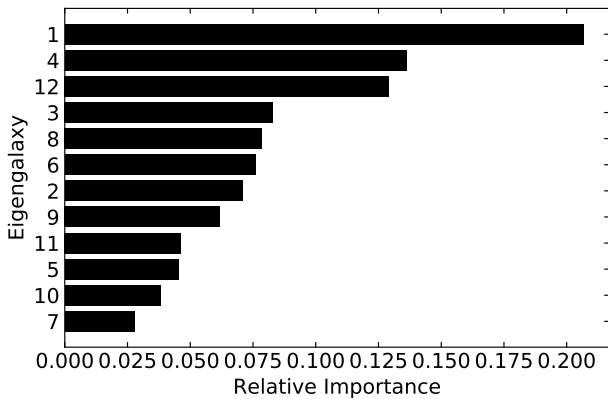


Figure 7. Importance weighting for each eigengalaxy in our random forest classifications. This shows a particular emphasis on eigengalaxies 1, 4 and 12 when classifying edge-on, spiral and clumpy galaxies against each other.

ing data in an expectation maximisation setting, and thus predict missing values and compute PCA at the same time². This enables PCA even when data is missing, and it also enables the prediction of missing values; (ii) given a generative factor model fitted within our eigengalaxy framework, we can assign a probability to the generation of any given galaxy

² Although not explored in this paper, we also note that PPCA makes a ‘mixture of PCAs’ model (Tipping & Bishop 1999a) possible. This enables the discovery of linear sub-spaces and the simultaneous PCA fitting of them, which may be more suited to datasets with which PCA struggles (e.g. data which cannot be well described by a mean and covariance structure). It may also reduce the overall dimensionality requirements for each linear sub-space compared to global PCA.

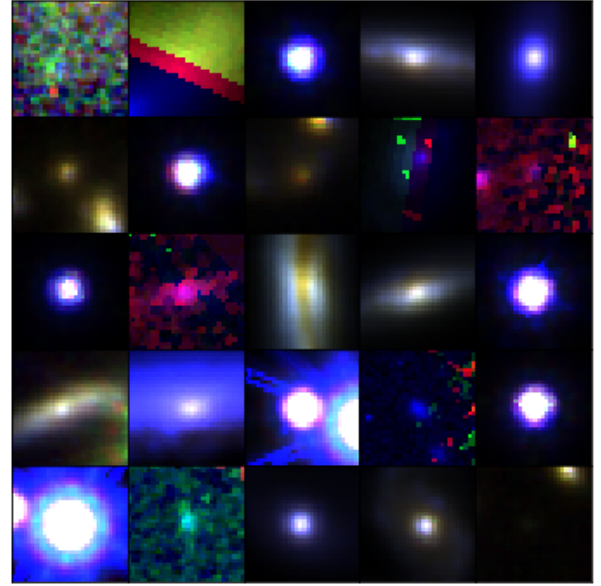


Figure 8. 25 of the ‘rarest’ galaxies from our sample. Rarity is quantified by the likelihood of the galaxy being generated by the PPCA generating function. The image shows anomalous detections and artefacts along with real, but intrinsically rare types of objects. Each 1.8” thumbnail image is an RGB composite of the F160W, F125W, and F814W bands.

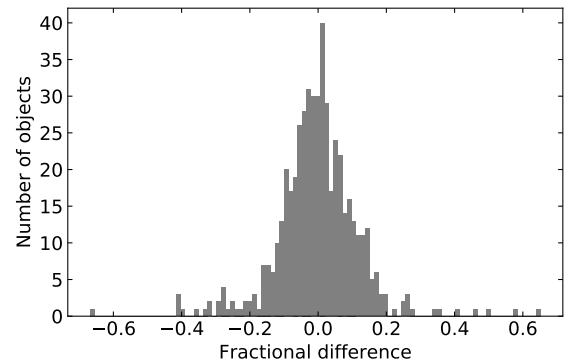


Figure 9. The frequency of the ratio of the sum of deltas (difference between the original and predicted pixel flux) and the sum of the flux of the original images for galaxies with missing data. The body of the distribution extends to $\pm 20\%$ error but $\sim 72\%$ of objects are predicted within $\pm 10\%$ error, indicating that PPCA can predict missing data in a 2D sense with a high level of fidelity.

x using the Gaussian density $p(x | \mu, WW^T + \sigma^2 I)$. Sorting galaxies by their likelihood therefore provides a natural measure of ‘rarity’ which may be used to identify outliers in a quantitative manner. In the next section, we explore some practical applications of these opportunities.

3 APPLICATIONS

In this section we explore some applications of the probabilistic eigengalaxy framework described above.

3.1 Outlier detection

A key utility of outlier detection is to make discoverable rare phenomena buried in enormous datasets. This may include searches for exotic galaxies and rare objects but also the identification of anomalous detections and pipeline errors. The two-part challenge is first to define an ‘outlier’ in a way useful to astronomy, and the second is to scale the detection algorithm to the size of the data.

Dutta et al. (2007) implement a distributed version of PCA using random projection and sampling to approximate eigenvectors for the purpose of outlier detection and apply it to the 2MASS (Skrutskie et al. 2006) and SDSS (Fukugita et al. 1996) datasets. In defining an outlier they search for galaxies which are over-represented by the last eigenvector. Other large scale PCA methods include incremental PCA (Ross et al. 2008), which approximates PCA by processing data in batches commensurate with the available random access memory. Baron & Poznanski (2017) utilise a random forest and fit to discriminate between real and synthetic data³. For every pair of objects, they count the number of trees in which each pair is labelled ‘real’ in the same leaf. The output is a $N \times N$ similarity matrix which is then searched for ‘outliers’, defined as objects with a large average distance from all other objects.

We focus on a simple and principled definition for an ‘outlier’, proceeding directly from our eigengalaxy framework. Given that PPCA allows us to cast our eigengalaxy result to a probabilistic model, a natural definition for an outlier is an object with a low probability of being generated. Outliers can thus be interpreted as the objects least representative of the object population described by the mean and covariance structure of the factor model. Note that the approach of calculating PCA for a set of features, converting it to PPCA and then using our outlier definition is general and could be applied not only to imaging, but also to spectroscopy, light curves, catalogues and other kinds of data. We define a formal outlier description within the eigengalaxy framework: given a generative factor model $N(Wx + \mu, \sigma^2 I)$, an outlier x is an object such that $p(x | Wx + \mu, \sigma^2 I) < T$ where T is a threshold probability density, and can be set according to the purpose at hand.

To illustrate the concept with the GZ-CANDELS dataset, we use our derived eigengalaxies to assign a log likelihood to every galaxy, using the `score_samples` method on the `sklearn.decomposition.PCA` object which implements the Tipping & Bishop (1999b) factor model representation to calculate likelihood. We sort the data by likelihood and present in Figure 8 the 25 objects least likely to be generated. The image shows not only anomalous detections and artefacts but also systems that are known to be rare, such as dust lanes which are signposts of recent minor mergers (see e.g. Kaviraj et al. 2012), ongoing mergers (see e.g. Darg et al. 2010) and edge-on spirals which appear to be accreting a blue companion. Outlier detection therefore offers an efficient way to identify examples of rare objects in large surveys.

3.2 Predicting missing data

In many situations one might be missing a particular band, for example due to bad data, partial coverage with a certain bandpass, obliteration by *Starlink* satellite trails, etc. In these cases we can consider how well we can predict the missing data using eigengalaxies. Tipping & Bishop (1999b) define an expectation maximisation (EM) algorithm for PPCA in the presence of missing data which works by treating missing values as jointly distributed with the latent variables and maximising the expectation of the joint likelihood function. As a demonstration, we randomly omit a band with equal probability from our dataset for 5% of rows chosen at random. We use the data as processed in Section 2.2 and an efficient variational EM version of the Tipping & Bishop (1999b) algorithm⁴ set out in Porta et al. (2005) to fit our PPCA model. We use the delta sum over flux sum ratio as in Figure 2 for the reconstruction error to describe the prediction error. Figure 9 illustrates the distribution of prediction error. The distribution is roughly symmetrical and is centred on zero. The body of the distribution extends to $\pm 20\%$ error but $\sim 72\%$ of objects are accounted for within $\pm 10\%$ error showing that high fidelity prediction is possible for most objects. Figure 10 provides some examples of predicted data for different bands. It is noteworthy that by using information contained in the eigengalaxies, PPCA is successful in estimating total flux even when it bears no resemblance to that of the other bands. The ability to predict missing images offers a route to ‘filling in’ missing data, such as predicting photometric data points which are absent in the observations in order to reconstruct missing parts of a galaxy’s SED.

3.3 Searching for galaxies similar to an exemplar

Given a survey with a large number of objects with diverse variety, and an interest in galaxies of a specific kind of object, it is useful to be able to present an exemplar galaxy and use it to quickly search for all other galaxies with similar features. The utility and suitability of a similarity search for any particular use case will depend primarily on how the objects are being described, and how the similarity between their descriptions is being calculated. For example, Protopapas et al. (2006) use cross-correlation as a proxy for similarity between light curves for the purpose of detecting outliers whereby light curves with the lowest average similarity are defined as outliers. Sart et al. (2010) utilise dynamic time warps (Berndt & Clifford 1994) to measure the similarity between light curves. Hocking et al. (2018) compare various measures, including Euclidean distance and Pearson’s correlation coefficient, and settle on using cosine distance to measure similarity from a description generated by growing neural gas prior to hierarchical clustering.

The eigengalaxy framework projects galaxies to real row vectors in an 12D space. The dimensions are not arbitrary but represent the eigengalaxies which together reconstruct the galaxies whilst preserving 96% of variance. Further, the value of each dimension is easy to interpret: it represents the weights required for each eigengalaxy to reconstruct the

³ These authors use the flux at each wavelength as a feature set, generating synthetic data by sampling from the marginal distribution of each feature.

⁴ Available in Python package `pyppca`.

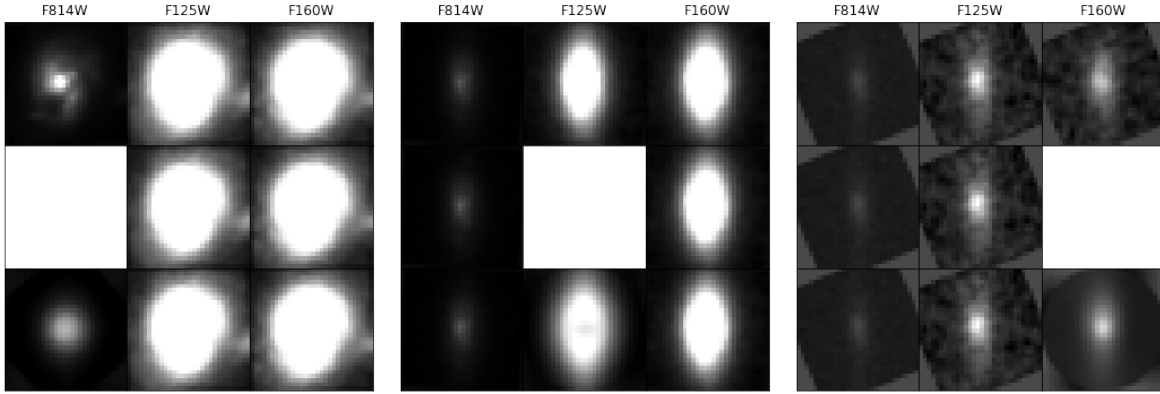


Figure 10. An example of using PPCA for image imputation. In each figure, the first row shows the original galaxy across all three bands, the second row shows the same galaxy with a random band censored, the third row shows the censored galaxy predicted by PPCA. It is noteworthy that by using information contained in the eigengalaxies, PPCA is successful in estimating brightness correctly even when it bears no resemblance to that of the other bands, as illustrated in the left most image.

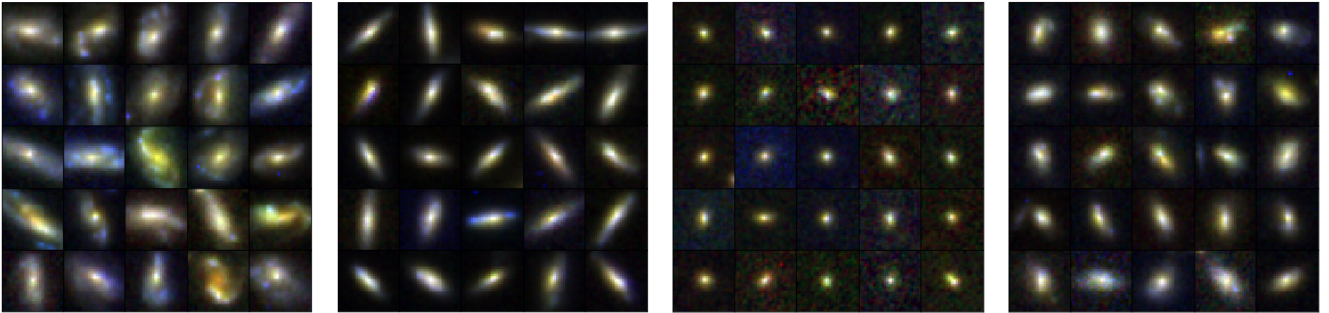


Figure 11. Examples of similarity searches. In each $1.8''$ thumbnail image (an RGB composite of the F160W, F125W, and F814W bands), the exemplar galaxy is given in the top left, followed by 24 of its nearest neighbours by Euclidean distance in the 12D eigengalaxy space. The image shows searches for spirals, edge-on spirals, ellipticals and recent mergers from left to right respectively.

original galaxies as a linear combination of eigengalaxies. The closer row-vector weights are to each other, the more similar their constitution in terms of eigengalaxies and thus the more similar their reconstruction. In this case, Euclidean distances are preferable over, say, cosine distance or a correlation measure, because we want to be sensitive primarily to the magnitude of row vector differences. Formally, let r be our exemplar galaxy expressed as a row vector and let X be our dataset (an $N \times 11$ matrix). Let Y represent the column vector of Euclidean distances of length N . Y_n is given by:

$$Y_n = \left(\sum_{i=1}^{11} (X_{n,i} - r_i)^2 \right)^{1/2}. \quad (1)$$

Let I be the indices of Y . We sort I with respect to the ascending order of Y , which gives us all objects in order of similarity to the exemplar. To demonstrate, we pick an exemplar galaxy and implement the procedure above. Figure 11 illustrates four examples of similarity searches, showing the 24 most similar galaxies to the exemplar. The image shows searches for spirals, edge-on spirals, ellipticals and recent mergers from left to right respectively. Most of the features are invariant to arbitrary brightness and the object registration has excluded aspects such as galaxy rotation, rendering this elementary algorithm remarkably effective.

3.4 Unsupervised clustering

Unsupervised clustering is particularly useful for massive astronomy datasets because it provides a method of investigating very large collections of objects efficiently. If the clustering method is effective at grouping objects with similar features together, then one can study a dataset by characterising its *morphological clusters* rather than examining each object separately. There is some precedence for this in astronomy. For example, [Martin et al. \(2020\)](#) follow [Hocking et al. \(2018\)](#) in using growing neural gas and hierarchical clustering directly on pixel data to identify structurally distinct clusters. [Almeida et al. \(2010\)](#) and [Almeida & Prieto \(2013\)](#) utilise k -means to classify spectra from SDSS into fewer base types. [Valenzuela & Pichara \(2018\)](#) use k -medoids⁵ to cluster and map sequences of light curve segments to variational trees.

The interpretation of the eigengalaxy framework described in Section 2.4 naturally extends to a simple unsupervised clustering treatment. We can create a distance matrix (an $N \times N$ matrix in which each cell indicates a distance be-

⁵ In k -medoids, data points become cluster centres, unlike k -means where the cluster centre is not necessarily correspondent to a data point.

tween object j at row j and object i at row i) by calculating the Euclidean distance between every galaxy. The distance matrix provides an input for a broad range of unsupervised clustering algorithms. This provides us with an opportunity to define and discover groups of galaxies based on the similarity of their multi-band morphologies as encoded by the eigengalaxies.

To demonstrate this, we produce a distance matrix for the GZ-CANDELS dataset as outlined above. We use affinity propagation (Dueck 2009) which produces 536 clusters from the total sample of 10,243 objects, with clusters varying in size from 1 to 316 with a median size of 4. Affinity propagation has a tunable ‘preference’ parameter that allows the coarseness of clustering to be adjusted; here we use the default value (the median of the distance matrix). Figure 12 illustrates samples of galaxies from four morphological clusters. It is noteworthy that affinity propagation is an exemplar-based algorithm, so that each cluster is actually characterised by an exemplar galaxy. Thus, in this instance the whole dataset is summarised by 536 exemplars (5% of the sample) which could, in principle, be sorted by rarity (see Section 3.1) and then viewed as one large image. This massive reduction in the scale of the full dataset highlights the efficiency gains that can be made by using this method for exploring the extremely large imaging surveys of the future.

3.5 Combining methods

All the methods described above utilise the same framework and can be used together to create additional capabilities simply based on the eigengalaxy weights in the score matrix. There are many possible combinations but we highlight three:

- Missing value prediction \rightarrow all methods. Predicting missing band values, dead pixels, etc. can be used to ‘complete’ data so that it may be considered on par with the rest of the data. It may then be used with any of the other methods.
- Outlier detection \rightarrow similarity search / clustering / classification. We may discover an interesting outlier (e.g. a rare object such as a gravitationally lensed galaxy) of which we would like to find many more examples (similarity search). We may want to cluster the outliers to determine a self-similar morphological clusters. We may also want to label a training set of outliers, train a classifier and then select only the outliers of interest.
- Clustering \rightarrow missing value prediction. To make the prediction of missing values more accurate, we may first generate eigengalaxies using the available bands and use it to create a clustering. This produces a set of self-similar classes to which missing values have more in common than the whole population. For each cluster we could then separately derive eigengalaxies and predict missing values for objects within that cluster.

3.6 Big data

The GZ-CANDELS dataset is relatively small and can be easily processed. In this section we consider problems and adaptations which may be necessary to use these methods

with extremely large datasets, such as LSST (Robertson et al. 2017), *Euclid* (Refregier et al. 2010) and the Square Kilometre Array (Weltman et al. 2020) which may contain billions of observed objects. We assert that the eigengalaxy framework offers a novel solution to processing such big data by making it possible to find outliers, search for and cluster objects using only the reduced score matrix form of a dataset. For example, if LSST was to provide a corresponding score matrix, eigengalaxies and galaxy likelihoods, all the methods described here would be available based on a small fraction of the full dataset.

An important consideration in making the methods presented here feasible for big data is the number of eigengalaxies required to achieve a practically useful level of explained variance. Aggarwal et al. (2001) provides a deeper discussion on common issues for algorithms operating in high dimensional space. In our case we would expect the following problems given too many eigengalaxies:

- (i) The score matrix form of the data may itself be too large to be useful. In our case, as the number of eigengalaxies approaches 10,243, the total size of the data converges onto the total size of the cut-out collection.
- (ii) Euclidean distance loses interpretability and the power to distinguish objects as the number of dimensions grows.
- (iii) Some techniques like fully calculating a distance matrix or calculating the similarity of every object with reference to an exemplar would not be computationally scalable.

Taking LSST as an example, we would expect that the number of eigengalaxies required to explain, say, 96% variance to be more than in our GZ-CANDELS experiments for two primary reasons: (i) it is a deeper survey and it therefore observes more low mass galaxies, the morphological mix of which is yet unknown (e.g. Martin et al. 2019), and (ii) we would expect bright galaxies to have more detail such as extended debris and tidal features (e.g. Duc et al. 2011) and therefore exhibit more variance. However, the additional sources of variance are limited, and we would expect a reasonable asymptotic number of eigengalaxies to emerge for useful level of explained variance at relatively small sample sizes.

The kind of variance that needs to be captured and the sufficient ratio of it to retain ultimately depends on the intended application. If the number of eigengalaxies is too high we could explore various ways to reduce the variance not required for the intended purpose in order to stay within an eigengalaxy quota at a useful explained variance ratio. Potentially applicable techniques include using smaller cut-outs, down-sampling pixels, using fewer bands, combining bands, stretching the range of the flux densities to make differences less subtle, and partitioning the data by some other variable (e.g. brightness, location, etc.) and then conducting the analysis per partition. If the number of eigengalaxies was workable from a data size perspective but a problem for Euclidean distance then we could use other distance measures more robust in high dimensional space. Finally, in every case we would need to replace exhaustive similarity searches with more scalable methods such as the nearest neighbour algorithm (Beis & Lowe 1997), and affinity propagation would need to be replaced with a less expensive clustering method

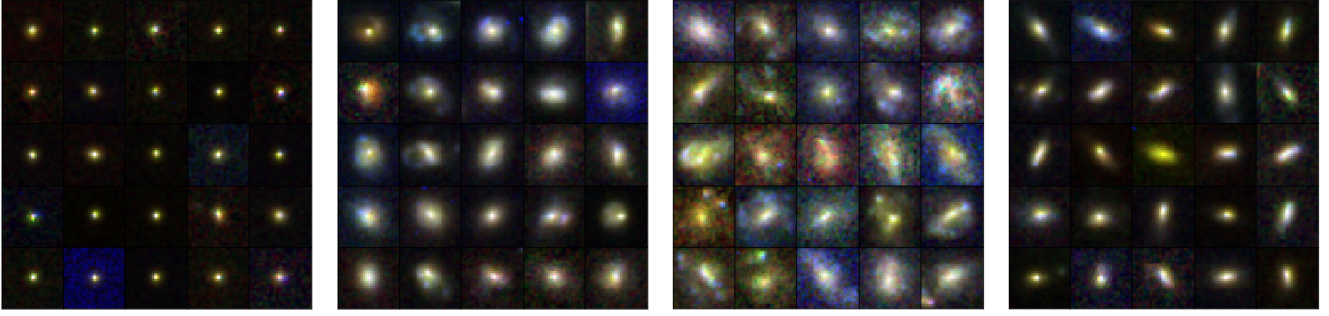


Figure 12. Composite image samples of four morphological clusters from a total of 536 created using affinity propagation clustering of a distance matrix defined by pairwise Euclidean distances in 12D eigengalaxy space. Each 1.8'' thumbnail image is an RGB composite of the F160W, F125W, and F814W bands.

such as k -means (or k -medoids if Euclidean distance was unacceptable).

4 CONCLUSIONS AND SUMMARY

We have demonstrated how a large sample of galaxies can be described in terms of a small set of template ‘eigengalaxies’. Eigengalaxies can be considered to be the image-space equivalent of ‘basis vectors’, interpreted as orthogonal features. This offers a completely data-driven approach to characterising galaxy morphology. Using a sample of 10,243 galaxies from the Galaxy Zoo–CANDELS survey, chosen to lie in the deep GOODS–S field, we use three-band *HST* ACS and WFC3 imaging to derive just 12 eigengalaxies that are sufficient to explain 96% of the morphological variance in the sample. How eigengalaxies correspond to real features in galaxies can be explored by examining samples where particular eigengalaxies are emphasized or de-emphasized. For example, we have shown how the eigengalaxies can be mapped to semantically convenient labels using Galaxy Zoo classifications. We have further shown how eigengalaxies can be embedded into a probabilistic framework and so enable a variety of useful applications. We explored four potential applications of our framework:

(i) we have shown how PPCA can be used to assign likelihoods and identify outliers as objects with a low probability of being generated.

(ii) we have shown how PPCA can be used to predict missing values in imaging, for example due to bad data or partial coverage in a given band.

(iii) we have shown how the projection of eigengalaxies on to a 12D space naturally facilitates similarity searches, where galaxies can be sorted relative to their Euclidean distance from an exemplar, thus quickly returning samples of galaxies that are morphologically similar to the exemplar as defined by their eigengalaxy components.

(iv) we have shown how the Euclidean distances between galaxies in the 12D space can be compiled into a distance matrix that can provide the input for unsupervised clustering algorithms to discover groups of similar objects. We have demonstrated this using affinity propagation to show how morphologically similar groupings can be identified in large samples.

Finally, we have described how the methods may be

used together in more advanced use cases and how working in eigengalaxy space may present a novel solution to outlier detection, as well as search and clustering problems in forthcoming massive imaging datasets such as LSST. We argue that these results and illustrations underscore the suitability of our PCA based probabilistic eigengalaxy framework for the study of morphology, especially in the era of big data astronomy, where representational efficiency and relevance will pay dividends.

Code for all results and figures can be found at <https://emiruz.com/eigengalaxies>.

ACKNOWLEDGEMENTS

J.E.G. is supported by the Royal Society. S.K acknowledges a Senior Research Fellowship from Worcester College Oxford. This work is based on observations taken by the CANDELS Multi-Cycle Treasury Program with the NASA/ESA *HST*, which is operated by the Association of Universities for Research in Astronomy, Inc., under NASA contract NAS5-26555. This research made use of Astropy,⁶ a community-developed core Python package for Astronomy (Astropy Collaboration et al. 2013; Price-Whelan et al. 2018).

REFERENCES

- Abraham R. G., Valdes F., Yee H. K. C., van den Bergh S., 1994, *ApJ*, **432**, 75
- Aggarwal C. C., Hinneburg A., Keim D. A., 2001, in International conference on database theory. pp 420–434
- Almeida J. S., Prieto C. A., 2013, *The Astrophysical Journal*, **763**, 50
- Almeida J. S., Aguerri J. A. L., Munoz-Tunón C., De Vicente A., 2010, *The Astrophysical Journal*, **714**, 487
- Anderson B., Moore A., Connolly A., Nichol R., 2004, in Proceedings of the tenth ACM SIGKDD international conference on Knowledge discovery and data mining. pp 40–48
- Astropy Collaboration et al., 2013, *A&A*, **558**, A33
- Bamford S. P., et al., 2009, *MNRAS*, **393**, 1324
- Baron D., Poznanski D., 2017, *Monthly Notices of the Royal Astronomical Society*, **465**, 4530
- Beck M. R., et al., 2018, *MNRAS*, **476**, 5516

⁶ <http://www.astropy.org>

- Beis J. S., Lowe D. G., 1997, in Proceedings of IEEE computer society conference on computer vision and pattern recognition. pp 1000–1006
- Berndt D. J., Clifford J., 1994, in KDD workshop. pp 359–370
- Bluck A. F. L., Mendel J. T., Ellison S. L., Moreno J., Simard L., Patton D. R., Starkenburg E., 2014, *MNRAS*, **441**, 599
- Bundy K., Ellis R. S., Conselice C. J., 2005, *ApJ*, **625**, 621
- Cappellari M., et al., 2011, *MNRAS*, **416**, 1680
- Cheng T.-Y., et al., 2019, arXiv e-prints, p. [arXiv:1908.03610](https://arxiv.org/abs/1908.03610)
- Codis S., Pichon C., Devriendt J., Slyz A., Pogosyan D., Dubois Y., Sousbie T., 2012, *MNRAS*, **427**, 3320
- Conselice C. J., 2003, *ApJS*, **147**, 1
- Conselice C. J., 2006, *ApJ*, **638**, 686
- Darg D. W., et al., 2010, *MNRAS*, **401**, 1043
- De La Calleja J., Fuentes O., 2004, Monthly Notices of the Royal Astronomical Society, **349**, 87
- Dieleman S., Willett K. W., Dambre J., 2015, *MNRAS*, **450**, 1441
- Djorgovski S. G., Mahabal A. A., Donalek C., Graham M. J., Drake A. J., Moghaddam B., Turmon M., 2012, arXiv e-prints,
- Dressler A., et al., 1997, *ApJ*, **490**, 577
- Duc P.-A., et al., 2011, *MNRAS*, **417**, 863
- Dueck D., 2009, Affinity propagation: clustering data by passing messages. Citeseer
- Dutta H., Giannella C., Borne K., Kargupta H., 2007, in Proceedings of the 2007 SIAM International Conference on Data Mining. pp 473–478
- Fukugita M., Shimasaku K., Ichikawa T., Gunn J., et al., 1996, Technical report, The Sloan digital sky survey photometric system. SCAN-9601313
- Goulding A. D., et al., 2018, *Publications of the Astronomical Society of Japan*, **70**, S37
- Grogin N. A., et al., 2011, The Astrophysical Journal Supplement Series, **197**, 35
- Hocking A., Geach J. E., Sun Y., Davey N., 2018, *MNRAS*, **473**, 1108
- Hubble E. P., 1926, *ApJ*, **64**, 321
- Huertas-Company M., et al., 2015, *ApJS*, **221**, 8
- Jackson R. A., Martin G., Kaviraj S., Laigle C., Devriendt J. E. G., Dubois Y., Pichon C., 2019, *MNRAS*, **489**, 4679
- Jackson R. A., Martin G., Kaviraj S., Laigle C., Devriendt J., Dubois Y., Pichon C., 2020, arXiv e-prints, p. [arXiv:2004.00023](https://arxiv.org/abs/2004.00023)
- Kaviraj S., 2010, *MNRAS*, **406**, 382
- Kaviraj S., 2014, *MNRAS*, **440**, 2944
- Kaviraj S., et al., 2007, *ApJS*, **173**, 619
- Kaviraj S., et al., 2012, *MNRAS*, **423**, 49
- Kaviraj S., Devriendt J., Dubois Y., Slyz A., Welker C., Pichon C., Peirani S., Le Borgne D., 2015, *MNRAS*, **452**, 2845
- Kaviraj S., Martin G., Silk J., 2019, *MNRAS*, **489**, L12
- Koekemoer A. M., et al., 2011, The Astrophysical Journal Supplement Series, **197**, 36
- Lackner C. N., Gunn J. E., 2012, *MNRAS*, **421**, 2277
- Lahav O., et al., 1995, *Science*, **267**, 859
- Le Borgne J.-F., et al., 2003, *Astronomy & Astrophysics*, **402**, 433
- Li C., Wang T.-G., Zhou H.-Y., Dong X.-B., Cheng F.-Z., 2005, *The Astronomical Journal*, **129**, 669
- Liaw A., Wiener M., et al., 2002, *R news*, **2**, 18
- Lintott C., et al., 2011, *MNRAS*, **410**, 166
- Lotz J. M., Primack J., Madau P., 2004, *AJ*, **128**, 163
- Ma Z., et al., 2019, *The Astrophysical Journal Supplement Series*, **240**, 34
- Martin G., et al., 2018a, *MNRAS*, **476**, 2801
- Martin G., Kaviraj S., Devriendt J. E. G., Dubois Y., Pichon C., 2018b, *MNRAS*, **480**, 2266
- Martin G., et al., 2019, *MNRAS*, **485**, 796
- Martin G., Kaviraj S., Hocking A., Read S. C., Geach J. E., 2020, *MNRAS*, **491**, 1408
- Menanteau F., Ford H. C., Motta V., Benítez N., Martel A. R., Blakeslee J. P., Infante L., 2006, *AJ*, **131**, 208
- Menou K., 2018, arXiv e-prints, p. [arXiv:1811.06374](https://arxiv.org/abs/1811.06374)
- Odewahn S. C., Cohen S. H., Windhorst R. A., Philip N. S., 2002, *ApJ*, **568**, 539
- Ostrovski F., et al., 2017, *MNRAS*, **465**, 4325
- Peirani S., Crockett R. M., Geen S., Khochfar S., Kaviraj S., Silk J., 2010, *MNRAS*, **405**, 2327
- Peth M. A., et al., 2016, *MNRAS*, **458**, 963
- Porta J. M., Verbeek J. J., Kröse B. J., 2005, *Autonomous Robots*, **18**, 59
- Postman M., et al., 2005, *ApJ*, **623**, 721
- Price-Whelan A. M., et al., 2018, *AJ*, **156**, 123
- Protopapas P., Giammarco J., Faccioli L., Struble M., Dave R., Alcock C., 2006, Monthly Notices of the Royal Astronomical Society, **369**, 677
- Refregier A., Amara A., Kitching T. D., Rassat A., Scaramella R., Weller J., 2010, arXiv e-prints, p. [arXiv:1001.0061](https://arxiv.org/abs/1001.0061)
- Robertson B. E., et al., 2017, preprint, ([arXiv:1708.01617](https://arxiv.org/abs/1708.01617))
- Ross D. A., Lim J., Lin R.-S., Yang M.-H., 2008, *International journal of computer vision*, **77**, 125
- Sart D., Mueen A., Najjar W., Keogh E., Niennattrakul V., 2010, in 2010 IEEE International Conference on Data Mining. pp 1001–1006
- Scarlata C., et al., 2007, *ApJS*, **172**, 406
- Schawinski K., et al., 2014, *MNRAS*, **440**, 889
- Schawinski K., Zhang C., Zhang H., Fowler L., Santhanam G. K., 2017, *MNRAS*, **467**, L110
- Sérsic J. L., 1963, *Boletín de la Asociacion Argentina de Astronomia La Plata Argentina*, **6**, 41
- Simard L., et al., 2002, *ApJS*, **142**, 1
- Simmons B. D., et al., 2016, Monthly Notices of the Royal Astronomical Society, p. [stw2587](https://arxiv.org/abs/1605.02587)
- Simmons B. D., et al., 2017, *MNRAS*, **464**, 4420
- Sirovich L., Kirby M., 1987, *Josa a*, **4**, 519
- Skibba R. A., et al., 2009, *MNRAS*, **399**, 966
- Skrutskie M., et al., 2006, *The Astronomical Journal*, **131**, 1163
- Smethurst R. J., et al., 2015, *MNRAS*, **450**, 435
- Soo J., et al., 2018, *Monthly Notices of the Royal Astronomical Society*, **475**, 3613
- Strateva I., et al., 2001, *AJ*, **122**, 1861
- Tipping M. E., Bishop C. M., 1999a, *Neural computation*, **11**, 443
- Tipping M. E., Bishop C. M., 1999b, *Journal of the Royal Statistical Society: Series B (Statistical Methodology)*, **61**, 611
- Valenzuela L., Pichara K., 2018, Monthly Notices of the Royal Astronomical Society, **474**, 3259
- Walmsley M., Ferguson A. M. N., Mann R. G., Lintott C. J., 2019, *MNRAS*, **483**, 2968
- Weltman A., et al., 2020, *Publ. Astron. Soc. Australia*, **37**, e002
- Wild V., et al., 2014, Monthly Notices of the Royal Astronomical Society, **440**, 1880
- Willett K. W., et al., 2015, *MNRAS*, **449**, 820
- Willett K. W., et al., 2017, *MNRAS*, **464**, 4176
- Wollaeger R. T., et al., 2018, *MNRAS*, **478**, 3298
- de Vaucouleurs G., 1948, *Annales d'Astrophysique*, **11**, 247